ARTICLE OPEN

Diverse electronic and magnetic properties of CrS₂ enabling strain-controlled 2D lateral heterostructure spintronic devices

Kaiyun Chen[1], Junkai Deng [1✉], Yuan Yan[1,2], Qian Shi[1], Tieyan Chang[1], Xiangdong Ding [1], Jun Sun[1], Sen Yang [1✉] and Jefferson Zhe Liu [2✉]

Lateral heterostructures of two-dimensional (2D) materials, integrating different phases or materials into a single piece of nanosheet, have attracted intensive research interests for electronic devices. Extending the 2D lateral heterostructures to spintronics demands more diverse electromagnetic properties of 2D materials. In this paper, using density functional theory calculations, we survey all IV, V, and VI group transition metal dichalcogenides (TMDs) and discover that CrS₂ has the most diverse electronic and magnetic properties: antiferromagnetic (AFM) metallic 1T phase, non-magnetic (NM) semiconductor 2H phase, and ferromagnetic (FM) semiconductor 1T′ phase with a Curie temperature of ~1000 K. Interestingly, we find that a tensile or compressive strain can turn the 1T′ phase into a spin-up or spin-down half-metal. Such strain tunability can be attributed to the lattice deformation under tensile/compressive strain that selectively promotes the spin-up/spin-down VBM (valence band bottom) orbital interactions. The diverse electromagnetic properties and the strain tunability enable strain-controlled spintronic devices using a single piece of CrS₂ nanosheet with improved energy efficiency. As a demo, a prototypical design of the spin-valve logic device is presented. It offers a promising solution to address the challenge of high energy consumption in miniaturized spintronic devices.

INTRODUCTION

Spintronics utilizes two intrinsic properties of electrons, spin and charge, to represent information compared to conventional charge-based electronics devices[1,2]. It is recognized as one of the most important research areas with an immense potential to provide logic and memory electronic devices with high speed, low power, and high density[3–6]. Magnetoresistive random access memory (MRAM) is the most promising spintronic device[7,8]. The basic structure of MRAM is a spin valve—a three-layer sandwich structure consisted of two ferromagnetic (FM) layers on two sides and one non-FM interlayer in the middle. The parallel or antiparallel magnetization of two FM layers generates a low or high resistance, designated as '1' or '0' bit. The writing operation is done via applying a magnetic field or using spin-torque transfer to control the magnetism of the two FM layers[9,10]. These methods require a high-density current flowing in the device, which causes high energy consumption and reduced reliability from generated high temperature. A lower energy spin valve is a challenge in spintronics miniaturization.[11]

There have been many efforts to employ electric fields to replace magnetic fields or spin-torque transfer for a low-energy spin valve. Some previous works showed that the coercivity and the magnetization could be changed under an electric field, e.g., voltage-controlled magnetoresistance in CoFeB/MgO/CoFeB[12,13]. Unfortunately, a bias magnetic field is still required, and the voltage applied to the devices are close to the breakdown voltage. Another option is to employ multiferroic materials. But, the ferroelectricity or multiferroicity is hard to maintain in the thin interlayer of a spin valve with a thickness of just a few nanometers[14,15]. Recently, a concept is proposed to overcome these problems: a spin valve made of magnetostriction materials

on a ferroelectric (piezoelectric) substrate[16,17]. These devices could be regarded as a strain mediated spin valve. The working mechanism is to transfer a piezoelectric strain generated from the substrate to the FM layer to modify its magnetic easy-axis via the inverse magnetostriction effect. Such a strain-controlled spin valve has low energy consumption[18,19]. But these devices have complex structures (e.g., 11 layers of different materials)[16].

A two-dimensional (2D)-material lateral heterostructure, which combines different 2D materials or phases into a single piece of nanosheet, is a promising solution for low-energy spin valves[20]. The atomically sharp interfaces in the lateral heterostructure reduce electronic resistance[21,22]. The local regions of the lateral heterostructures can be regulated under certain external stimuli to create atomically sharp junction[23–25], enabling the working mechanisms (e.g., strain mediation) to control the spin current with high energy efficiency. To develop such spintronic devices, it is imperative to discover the 2D materials that possess all the required electromagnetic properties for spintronics. In this regard, the 2D transition metal dichalcogenide (TMD) is the most attractive candidate. The rich chemical diversity and multiple phases (2H, 1T, 1T′, and 1T″) of the TMD family deliver diverse electronic and magnetic properties[26], which in many cases are tunable by external stimuli [27,28].

In this paper, using density functional theory (DFT) calculation, we systematically survey all IV, V, and VI group TMDs. Our results show that CrS₂ has the most diverse electronic and magnetic properties required in spintronics, including antiferromagnetic (AFM) metallic 1T phase, non-magnetic semiconductor (NM-SC) 2H phase, and ferromagnetic semiconductor (FM-SC) 1T′ phase. The most interesting observation is that a tensile or compressive strain can turn 1T′ CrS₂ into a spin-up or spin-down half-metal,

[1]MOE Key Laboratory for Nonequilibrium Synthesis and Modulation of Condensed Matter, State Key Laboratory for Mechanical Behavior of Materials, Xi'an Jiaotong University, Xi'an 710049, China. [2]Department of Mechanical Engineering, The University of Melbourne, Parkville, VIC 3010, Australia. ✉email: junkai.deng@mail.xjtu.edu.cn; yangsen@mail.xjtu.edu.cn; zhe.liu@unimelb.edu.au
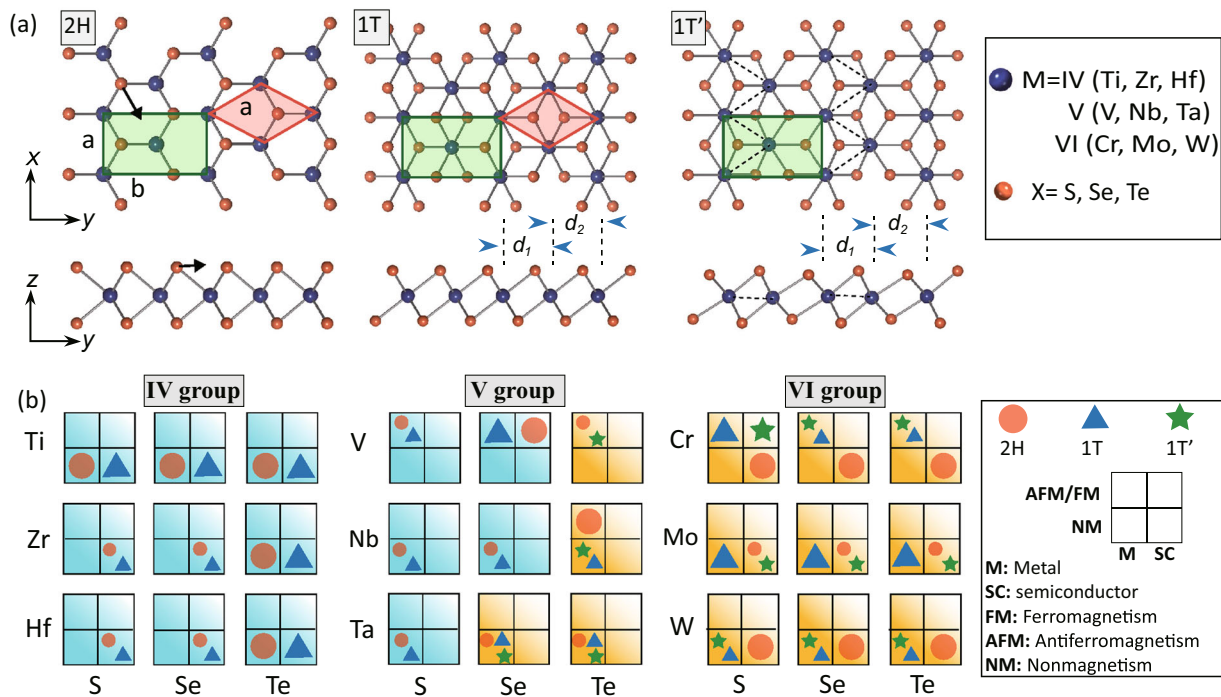
Fig. 1 Crystal structures and physical properties of 2H, 1T, and 1T' phase of group IV, V, and VI TMDs. a Crystal structures of 2H, 1T, and 1T'-CrS$_2$. The primitive unit of 2H and 1T are highlighted in orange rhombus. The primitive unit of 1T' corresponds to the 1 × √3 supercell of 2H and 1T that is highlighted in the green rectangle. The 2H phase can be derived via a collective top layer lateral slide to the center of hexagon denoted by the black arrow in the top view and side view. The 1T' phase can be derived via the structure distortion of 1T phase. These features are general in all TMDs monolayers. **b** Electronic and magnetic properties of IV, V, and VI TMDs. Note that CrS$_2$ has the most diverse properties, including antiferromagnetic metal, ferromagnetic semiconductor, and non-magnetic semiconductor corresponding to 1T, 1T', and 2H phases, respectively.

which was not observed in other 2D materials before. This feature allows strain engineering in different regions of a CrS$_2$ nanosheet to readily switch and match spin conduction channels for spin current control. As a demo, a prototype design of the spin-valve logic device is presented with the advantages of simple device structure and potentially low energy consumption.

RESULTS AND DISCUSSION

Electronic and magnetic properties of 2H, 1T, and 1T' phases of TMDs

Figure 1a depicts the crystal structure of 2H, 1T, and 1T' phase of TMDs (MX_2, M is the transition metal element and X is S, Se, or Te). The primitive unit cell of the 2H phase is a 120° rhombus with P63/mmc space group (the orange region in Fig. 1a). The 1T is a high-symmetry phase with P3$\overline{m}$1 space group and a 120° rhombus primitive cell. It can be transformed from the 2H phase via a collective sliding of the top layer X atoms to the hexagon center. The 1T' can be regarded as a distorted structure from the 1T phase, arising from the Peierls instability[29]. Peierls distortion is a primary mechanism for the formation of the 1T' phase in TMDs such as MoS$_2$ and MoTe$_2$[26,29,30]. For the metallic 1T phase, its super-structures will have a folded band structure. In some cases, a band continuously passes the Fermi level (E_f) exactly at one zone boundary, leading to the so-called Peierls instability. This will promote a spontaneous lattice distortion to open a small bandgap at the zone boundary. The primitive cell of 1T' is a rectangular unit, corresponding to a (1 × √3 × 1) supercell of the 1T phase (green rectangle in Fig. 1a). Compared with the 1T phase, two adjacent lines of metal atoms in the high-symmetry y-direction move toward each other to form a zig–zag M–M dimer chain (the dashed lines in Fig. 1a). Hence the distance between the adjacent metal atom lines (along y-direction) are not equal in 1T' phase: $d_1/d_2 < 1$,

different from a 1T phase having $d_1/d_2 = 1$. For a consistent comparison, all our DFT calculations for the 2H, 1T, and 1T' phases were based on the rectangular unit cell.

We carried out a comprehensive computational survey of the 2H, 1T, and 1T' phases of all group IV, V, and VI TMDs. The relative total energies of these three phases and their magnetic properties are shown in Supplementary Fig. 1a–c. A clear trend can be observed. For group IV TMD, 1T is the most stable phase, and the 1T' phase does not exist. As moving to the right of the periodic table, i.e., M atoms changing to the V and VI groups, the 1T' phase appears, and the 2H phase becomes the ground state for most TMDs. All three phases can exist in the group VI TMDs. In addition, as we move from group IV to group VI, more diverse magnetic properties can be observed, as shown in Supplementary Fig. 1d–f. All compounds in group IV TMDs are NM. Both ferromagnetism (FM) and antiferromagnetism (AFM) can be observed in group IV and VI TMDs such as FM-1T-VS$_2$ and AFM-1T-CrS$_2$. Figure 1b summarizes all results, including (mechanical) stable phases, electronic conductivity, and magnetism. The blue background highlights the TMD cases with stable 2H and 1T phases, and the orange background represents the TMD cases with three stable phases. A clear boundary exists in the group V TMDs.

There are four different types of combination of electronic conductivity (metal vs. semiconductor) and magnetism (NM vs. AFM/FM). Among all TMDs in Fig. 1b, CrS$_2$ is a special one with the most diverse electronic/magnetic properties, i.e., three out of the four possible combinations in its three different phases. The electronic band structures calculated using HSE06 functional for the 2H, 1T, and 1T' CrS$_2$ are shown in Supplementary Fig. 2a, b and Fig. 2a, respectively. A comprehensive comparison of total energy values of different magnetic orders of 1T and 1T' phase is presented in Supplementary Note 2. The 2H-CrS$_2$ is the NM-SC, and 1T-CrS$_2$ is the antiferromagnetic metal (AFM-M), which agrees
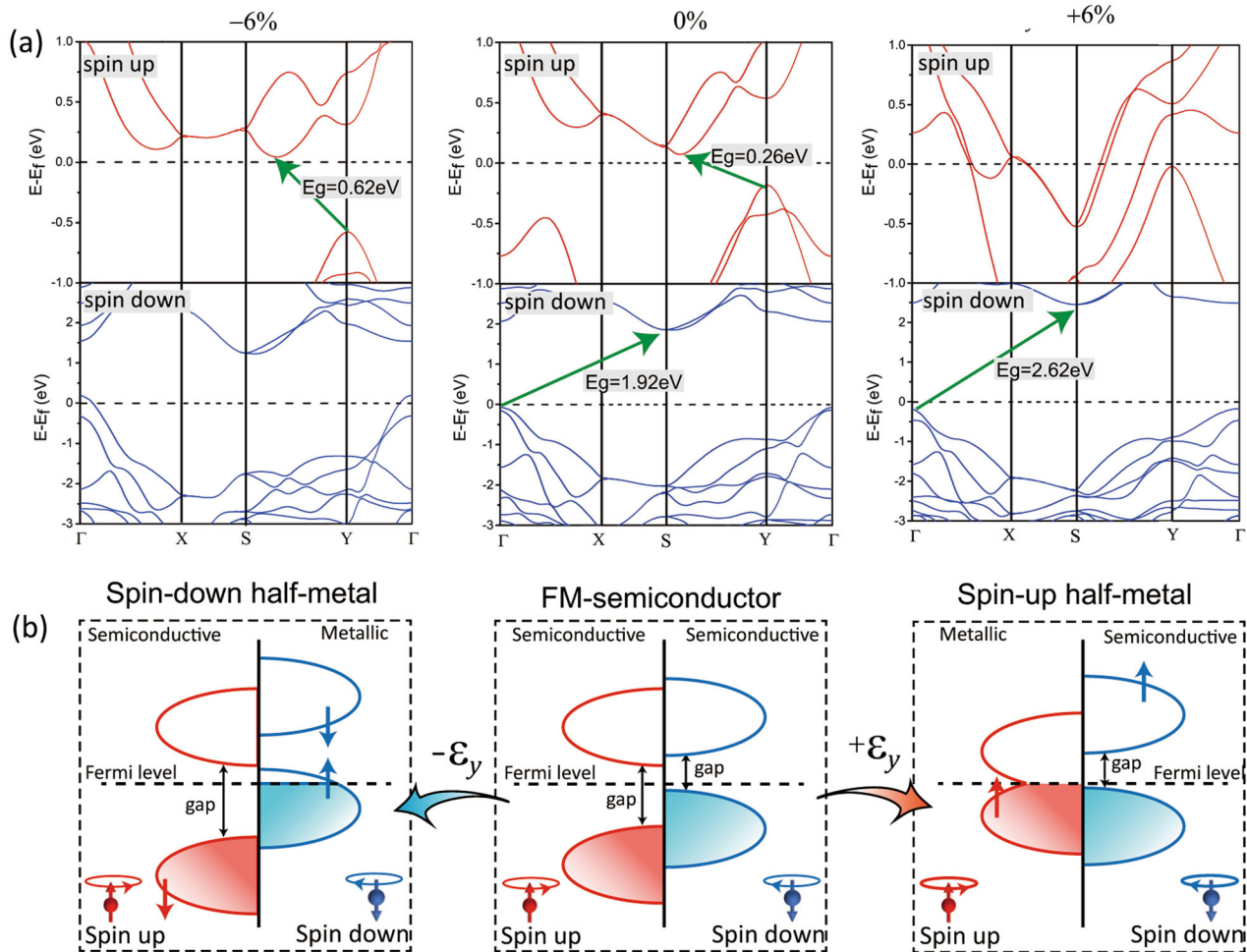
Fig. 2 Electronic band structures of 1T'-CrS$_2$ under different strains along the y-direction. a spin-polarized band structure of 1T' phase under −6%, 0%, and +6% strain along the y-direction calculated by using HSE06. The spin-up bandgap disappears under +6% strain while the spin-down gap disappears under −6% strain, corresponding to spin-up half-metallic and spin-down half-metallic states, respectively. The band structures at other strain are summarized in Supplementary Fig. 7. **b** A diagram to illustrate electron structure changes under tensile (+ε_y) and compressive (−ε_y) strain. The tensile strain causes spin-up VBM and CBM shifting upward and downward, respectively. The CBM will cross the Fermi level, transforming 1T'-CrS$_2$ to spin-up half-metal. The compressive strain causes spin-down VBM shifting upward and cross the Fermi level, transforming 1T'-CrS$_2$ to spin-down half-metal.

Table 1.	Lattice constants, magnetic order, and relative energy of 2H, 1T, and 1T' phases of CrS$_2$.								
Phase	Structure information				Bandgap (eV)		Magnetism	ΔE (eV per f.u.)	
	a(Å)	b(Å)	d_1	d_2	Spin up	Spin down		PBE	HSE06
2H	3.04	5.26			1.35	1.35	NM	0	0
1T	3.28	5.40	3.16	3.16	0	0	AFM	0.3734	0.7642
1T'	3.32	5.62	2.99	3.55	0.26	1.92	FM	0.3436	0.7149

PBE Perdew–Burke–Ernzerhof functional, *HSE* Heyd–Scuseria–Ernzerhof functional, *NM* non-magnetic, *AFM* antiferromagnetic, *FM* ferromagnetic.

with previous studies[31,32]. The CrS$_2$ 1T' phase is a FM-SC. Table 1 lists the crystal structure, magnetism, bandgap, and relative total energy results of the three different CrS$_2$ phases, 2H (NM-SC), 1T (AFM-M), and 1T' (FM-SC).

A recent experiment observed these three phases (2H, 1T, and 1T') of CrS$_2$ under ambient conditions[33]. Their DFT computational study, however, reported 1T'-CrS$_2$ as a NM semimetal by using the Perdew–Burke–Ernzerhof (PBE) and Heyd–Scuseria–Ernzerhof (HSE06) functionals. Our comprehensive PBE and HSE06 calculations concluded the FM-SC as the ground state of the 1T' phase

(Supplementary Note 3). Our result is also consistent with the measured low carrier mobility (~0.005 cm^2 V^{-1} s^{-1}) in the experiment.

In light of the importance of FM/AFM states in spintronics, we provide some in-depth analysis of the magnetic properties of the 1T and 1T' CrS$_2$. We compared the partial density of states' (PDOS) results of Cr d and S p electrons for these two phases in Supplementary Fig. 5. For the 1T phase, the Cr d orbital is spin-polarized, making the main contribution (2.664 μ_B per Cr atom) to the total magnetism, whereas S atoms have very weak magnetic

moments of $0.042\,\mu_B$. The magnetic interactions between two adjacent lines of Cr atoms should be the direct-exchange interaction[28,34]. For the 1T′ phase, Supplementary Fig. 5b shows strong hybridization between Cr d and S p orbitals. The magnetic moment of S atoms significantly increases to $0.326\,\mu_B$. The enhanced magnetic moments of S atoms and their opposite signs to those of Cr atoms suggest the super-exchange interaction (Cr–S–Cr interaction) in the 1T′ phase. The detailed analysis and description for the transition between direct-exchange and super-exchange are presented in Supplementary Note 2.
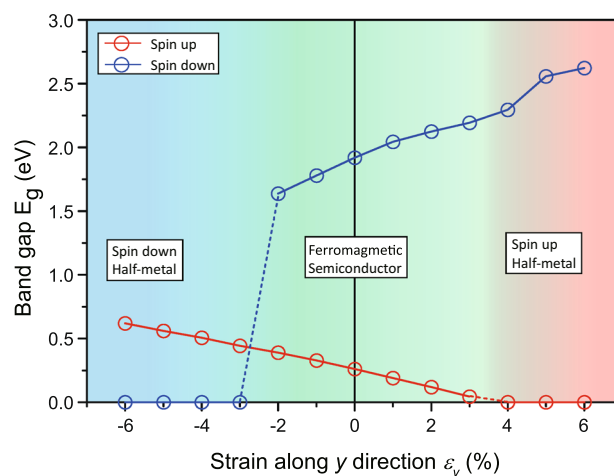
Strain-controlled half-metal switching in 1T′-FM-CrS$_2$

On top of the most diverse electronic/magnetic properties of CrS$_2$ among all TMDs, we also found that strain can transform the FM-SC 1T′ phase into spin-up and spin-down half-metals. Half-metals are essential for high-purity spin current in spintronics.

We applied a uniaxial strain along the y-direction ($-6\% < \varepsilon_y < +6\%$) on 1T′-CrS$_2$ in DFT calculations (details in section 'Methods'). Figure 2 shows the calculated band structures of the strained 1T′ phases using the HSE06 functional. The left figure in Fig. 2a shows that a compressive strain ($\varepsilon_y = -6\%$) closes the spin-down electron bandgap from 1.92 to 0 eV but open the spin-up bandgap from 0.26 to 0.62 eV. In contrast, the right figure in Fig. 2a shows that the tensile strain ($\varepsilon_y = +6\%$) closes the spin-up bandgap from 0.26 to 0 eV but open the spin-down bandgap from 1.92 to 2.62 eV. As such, a compressive or tensile strain can transform the 1T′-CrS$_2$ into spin-down or spin-up half-metal from a FM-SC. Supplementary Fig. 7 also shows the calculated band structures as strain from -6% to 9% using the PBE functional. The same conclusion can be drawn.

To understand the transition, we calculated the band structures of 1T′ CrS$_2$ under a series of uniaxial strains from -5% to $+5\%$. In Supplementary Fig. 8, the valence band bottom (VBM) and conduction band bottom (CBM) of the spin-up and spin-down electrons gradually shift upon strain changing. The trend is depicted in Fig. 2b. Applying a compressive strain causes the spin-down VBM shifting upward and the CBM shifting downward, narrowing the bandgap. At $\varepsilon_y \sim -2\%$, the spin-down VBM crosses the Fermi level, transforming the 1T′-CrS$_2$ into a spin-down half-metal. As for the spin-up electron, the VBM shifts downward to open up the bandgap. In contrast, as the applied tensile strain increased, the spin-up VBM moves upward, and the CBM level slightly moves downward. Under a strain $\varepsilon_y > 3\%$, the spin-up VBM and CBM cross the Fermi level, transforming 1T′-CrS$_2$ to spin-up half-metal. Meanwhile, the spin-down CBM level moves upward to open the bandgap. Usually, to transform a semiconductor into a spin-down half-metal while keeping the total number of electrons in the unit cell the same, at least two different bands should cross the Fermi level. Any states emptied out by being pushed above the Fermi level under strain should be compensated for by other previously empty states becoming occupied. Our results are not the case. For example, under negative strains, only spin-down VBM crosses the Fermi level. This is because some electrons transfer from the spin-down state to the spin-up state, i.e., $0.00215e$ at -6% strain, to conserve the electron number. The detailed analysis is shown in Supplementary Note 4.

In Fig. 3, we summarize the bandgaps of the spin-up and spin-down electrons as a function of uniaxial strain ε_y. Three zones correspond to different electromagnetic properties of 1T′-CrS$_2$. In the blue zone ($\varepsilon_y < -2\%$), the strained 1T′-CrS$_2$ is a spin-down half-metal. In the green zone where strain is between -2% and 3%, the 1T′-CrS$_2$ remains as an FM semiconductor. When the tensile strain is higher than 3% (the red zone), it becomes a spin-up half-metal. Using strain engineering to transform 2D materials among the FM semiconductor, the spin-up half-metal, and the spin-down half-metal has not been reported before. A previous computational study showed that using a tensile strain of 10% could
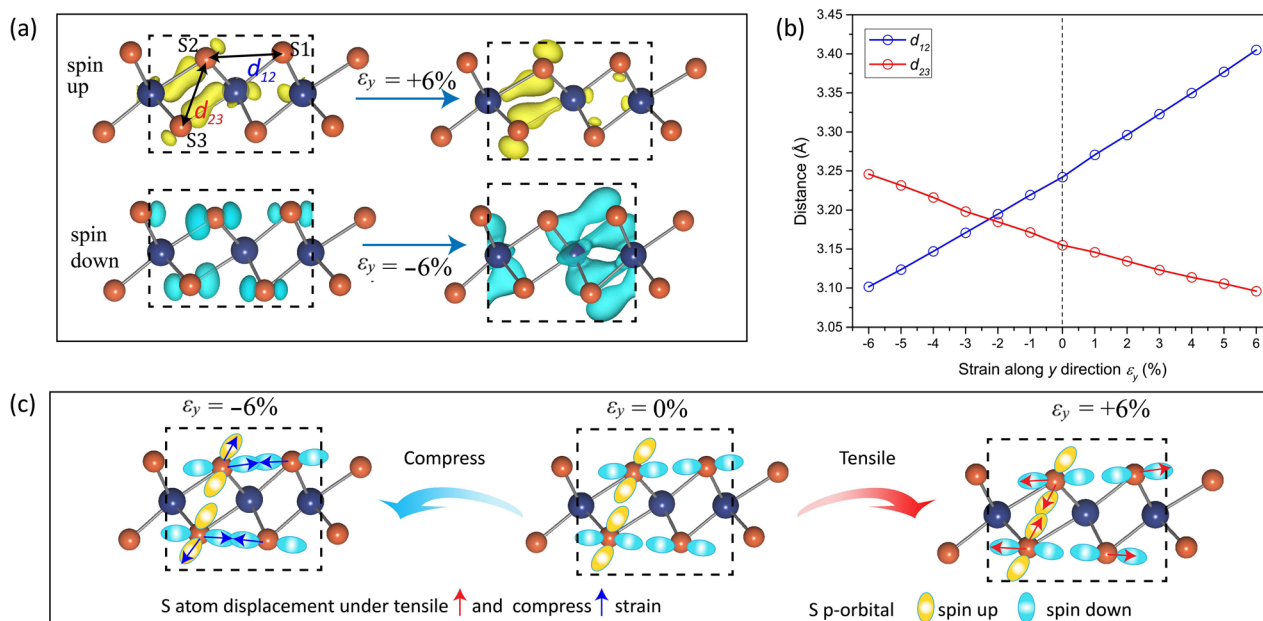
transform 1T-CrSe$_2$ from an FM metal to a spin-up half-metal[28]. But no spin-down metal property was reported. The 1T′-CrS$_2$ is the only TMD material with such tunable electromagnetic properties, which is critical for spintronic applications. Note that the required strains for property transition, –2% and 3%, have been achieved in experiments for different types of 2D materials[35,36].

To investigate the physical mechanism of the strain-induced half-metal transition, we decomposed the spin-up and spin-down electronic structures of 1T′-CrS$_2$ under $\varepsilon_y = -6\%$, 0%, and +6% in Supplementary Fig. 10. Our analysis shows that the continuous shift of VBM levels under strains leads to the FM-SC/half-metal transition (Fig. 2 and Supplementary Fig. 7). Understanding how crystal deformation influences the VBM levels should be the key. Decomposed electronic bands (Supplementary Fig. 10) and partial charge density (Fig. 4a) indicates that the VBM levels are mainly contributed from the S atoms. The spin-up VBM charge density (mainly around the S2 and S3 atoms) is distributed along with the Cr–S bonds across the CrS$_2$ monolayer. Under a tensile strain, the interatomic distances between S2 and S3 atoms (one on the top atomic layer and the other in the bottom atomic layer) are reduced significantly (Fig. 4b). As depicted in Fig. 4c, the spin-up VBM electron clouds on S2 and S3 atoms would move closer, resulting in stronger interactions. The charge density distribution of the 1T′-CrS$_2$ under +6% strain in Fig. 4a suggests a repelling interaction nature. As a result, the spin-up VBM level moves upward (Fig. 2b). Under a sufficiently large tensile strain ($\varepsilon_y > 3\%$), the spin-up VBM level will cross the Fermi level, transforming 1T′-CrS$_2$ to a spin-up half-metal. Since a tensile strain increases the interatomic distances between S atoms along the monolayer (i.e., d_{12} and d_{13}), the spin-down VBM electron clouds move away from each other (Fig. 4c). This could be the reason why the spin-down VBM level shows little shift in Fig. 2b.

Similar understanding can be applied for the compressive strain-induced spin-down half-metal transition. In Fig. 4b, a compressive strain reduces the interatomic distances between S atoms along the monolayer (i.e., d_{12} and d_{13}). The spin-down VBM electron clouds, which orientate along the CrS$_2$ monolayer, move closer (Fig. 4c). The repelling interaction shifts the VBM energy level (Fig. 2b) upward. Under a sufficiently large compressive

Fig. 3 Strain engineering to transform 1T′-CrS$_2$ from FM semiconductor to spin-up half-metal or spin-down half-metal states. Bandgap E_g of spin-up and spin-down electrons as a function of mechanical strain in the y-direction. At strain-free state, 1T′-CrS$_2$ in an FM semiconductor with spin-up $E_g \sim 0.26$ eV and spin-down $E_g \sim 1.92$ eV. Applying a positive strain ε_y leads to a reduction of spin-up E_g and increase of spin-down E_g. At $\varepsilon_y \sim +4\%$, the spin-up E_g diminishes, i.e., a spin-up half-metal state. Appling negative ε_y leads to an opposite trend. At $\varepsilon_y \sim -3\%$, spin-down E_g closes, i.e., spin-down half-metal.

Fig. 4 The crystal and electronic structures analysis to reveal the mechanism of strain-induced spin-up and spin-down half-metal switching of 1T′-CrS$_2$. a The electron charge density of spin-up and spin-down VBM of CrS$_2$ changes under ±6% strain (isosurface value is 10^{-3} e·bohr^{-3}). Both spin-up and spin-down VBM electrons mainly concentrate on S atoms. The spin-up electrons are distributed around the Cr–S bond across the monolayer. The spin-down electrons are distributed along the monolayer. **b** The distance of S1–S2 (d_{12}) and S2–S3 (d_{23}) varying with strain from −6% to +6% in the y-direction. **c** A diagram to demonstrate the change of spin-polarized VBM orbitals under either tensile or compressive strain. Under tensile strain, the spin-up VBM orbitals on S2 and S3 tend to overlap owing to decreased d_{23}, which causes the VBM levels cross the Fermi level. Under compressive strain, the spin-down VBM orbitals on S1 and S2 atoms tend to overlap owing to the decreased d_{12}, which causes the VBM levels cross the Fermi level.

strain ($\varepsilon_y < -2\%$), the spin-down VBM level will cross the Fermi level, transforming 1T′-CrS$_2$ to a spin-down half-metal. Again, a compressive strain increases the S2–S3 distance, and the spin-up VBM electron clouds move away from each other. There is little shift of spin-up VBM energy level in Fig. 2b. The lattice deformation under tensile/compressive strain selectively promotes the spin-up/spin-down VBM orbital interactions, leading to the observed strain-modulated spin-up/spin-down half-metal transition.

Phase and magnetic-state stability under strain

To utilize the strain-tunable electronic and magnetic properties of CrS$_2$ in 2D lateral heterostructure applications, we should study the stability of different phases and their magnetic states under strains and at ambient conditions.

The relative total energy of the 2H (NM-SC), 1T (AFM-M), and 1T′ (FM-SC and half-metal) phases as a function of uniaxial strain along the y-direction is shown in Fig. 5a. Here the lattice constants of the 1T′ phase are taken as references to calculate the strain. The 2H phase is the most stable phase in the strain range from −8% to −1.5%. As $\varepsilon_y > -1.5\%$, 1T′ is the most stable phase. The 1T phase has lower total energy than the 1T′ phase given $\varepsilon_y < -3.4\%$.

The 1T′ phase should be stable at least in the strain range of ∼ $-2\% < \varepsilon_y < 4\%$ (Fig. 3) to undergo the FM-SC/half-metal transition in applications. Figure 5a shows 1T′ as the ground state in the strain range of $-1.5\% < \varepsilon_y < 6\%$. Thus, we should consider the stability of 1T′ relative to 2H in the strain range of $-2\% < \varepsilon_y < -1.5\%$. We applied the climbing image nudged elastic band (CI-NEB) method to calculate the energy barrier for the 1T′–2H phase transition under different uniaxial strains (Fig. 5b). Under a compressive strain (up to –6%), the energy barrier is nearly a constant ∼0.6 eV per f.u., which is high enough to ensure the stability of 1T′ at room temperature. For the strain range of interest, the 1T′ phase is always stable under ambient conditions.

A large strain could alternate the magnetic ground states of CrS$_2$. We calculated the relative energy of different magnetic states of 1T and 1T′ phases as a function of uniaxial strain ε_y in Supplementary Fig. 13. The 1T′ always has the ground magnetic state as either FM-SC or half-metal. For the 1T phase, AFM is not a ground magnetic state only under a large tensile strain (>7%). Within the strain range of interest, there are no changes in the magnetic ground state of the 1T and 1T′ phases.

The Curie temperature (T_C) of FM semiconductor or half-metal is an essential parameter for spintronics applications. It is desirable to have T_C higher than room temperature. We adopted the Heisenberg model to estimate the T_C of 1T′-CrS$_2$ as in previous studies[28,37–39]. The calculation details are shown in Supplementary Note 8. In Fig. 5c, as ε_y changes from −6% to 6%, the T_C of 1T′ phase varies between ∼377.3 K and ∼1358.1 K, always higher than room temperature. This is not a surprise since previous works indicated that Cr compounds often had a higher T_C such as CrTe$_2$ and CrX (C, P, As, Sb)[28,34,37,40]. We should be aware that the Heisenberg model tends to overestimate T_C. However, it is still widely adopted for its simplicity and generally correct trend[28,37–39]. Besides, we also note that for CrTe$_2$[34], the T_C is about 310 K in the experiment, which is higher than the estimated value ∼219 K by the Heisenberg model[28]. Our primary focus is whether the Curie temperature of 1T′-CrS$_2$ (under strain ∼ $-3\% < \varepsilon < 4\%$) is higher than room temperature. The high T_C value (>800 K) from the Heisenberg model suggests the FM/half-metal state of 1T′ should be stable under the ambient condition.

Strain-controlled spintronics device designs

Among the popular spintronic devices such as magnetic field sensors, read heads for hard drives, galvanic isolators, and MRAM[1,7,41,42], the core component is a spin valve. The conventional basic structure of a spin valve has three components: two FM layers sandwiched with one NM interlayer. In light of its 100% spin polarization ratio, half-metal is the most attractive candidate
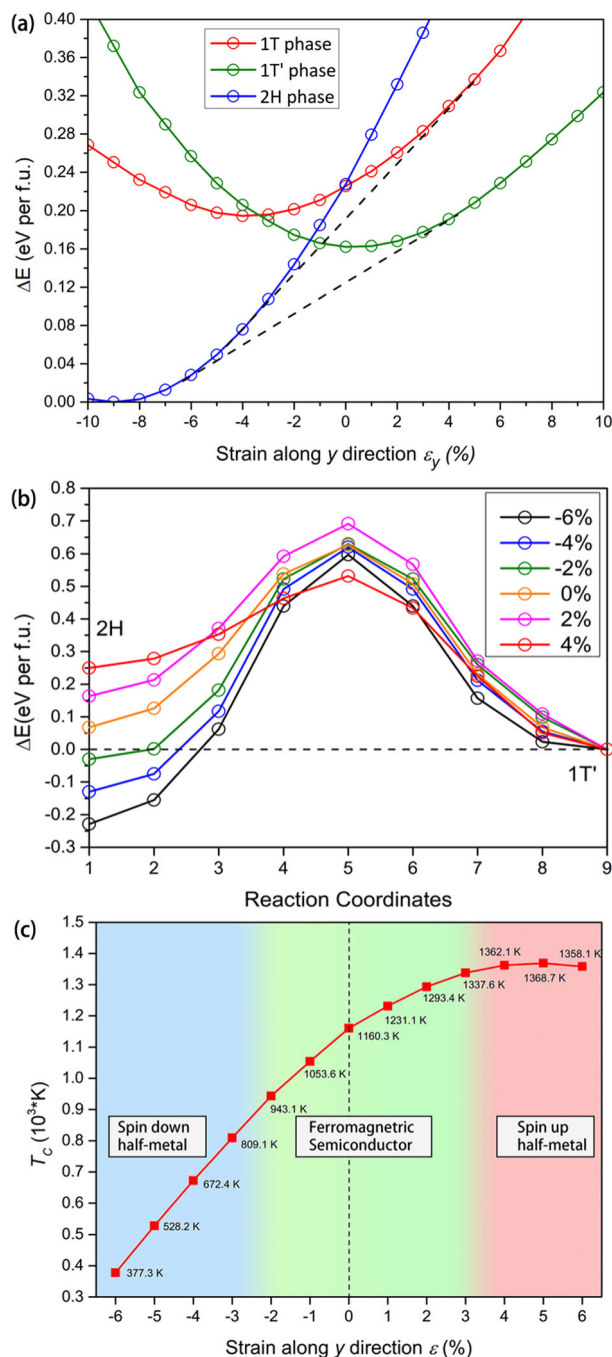
Fig. 5 Phase stability and transition between 1T, 1T', and 2H-CrS$_2$.
a The relative total energy of 2H, 1T, and 1T' phases as a function of uniaxial strain along the y-direction. The strain is defined with the equilibrium state of the 1T' phase. The dashed lines are the common tangents. **b** The phase transition pathway between 2H and 1T' under $\varepsilon_y = -6\%$, -4%, -2%, 0%, 2%, and 4% from NEB calculations. The results show substantial energy barriers to separate the 2H and 1T' phases. **c** Curie temperature (T_C) of 1T'-CrS$_2$ under y-direction strain. The semiconductor T_C is from 943.1 K to 1337.6 K, as strain changes from -2% to 3%. It means that ferromagnetic order could relatively exit under room temperature.

for the two FM layers[43,44]. The interlayer can be either a conductor or an insulator[1,42].

The diverse electron/magnetic properties of CrS$_2$, particularly the strain-induced spin-up and spin-down half-metal transition, offer a promising possibility to integrate the required three

components on a single piece of CrS$_2$ nanosheet for a 2D lateral heterostructure spin valve. In this heterostructure, the 1T' phase (under strain) can serve as the two FM layers, and the interlayer component can be either 1T-CrS$_2$ (metallic) or 2H CrS$_2$ (semiconductor). A simple design of strain-controlled two-channel (denoted as I and II) spin-valve logic device is demonstrated in Fig. 6. This is in an analogy to the nonvolatility, infinite endurance, and fast random-access logic device ('universal memory' MRAM) that is composed of an array of spin valves (multi-channels)[8].

The CrS$_2$ spin-valve device in Fig. 6 can be operated using strain instead of external magnetic fields. Supplementary Fig. 15a depicts the CBM and VBM levels of strained 1T'-CrS$_2$ compared with those of 1T and 2H phases. The CBM of the 2H phase is always higher than that of the strained 1T'. The 2H phase interlayer could effectively separate two half-metal layers as required in the tunneling magnetoresistance spin valve. Besides, the CBM/VBM of the 1T interface is always lower than that of the strained 1T' phase, as required in the giant magnetoresistance spin valve. The band alignments of CrS$_2$ in different phases (under strain-control), therefore, satisfy basic requirements in a spin valve. When applying the same strains on the two FM layers, both of them will be either spin-up or spin-down half-metal. As a result, only the spin-up or spin-down electrons could be conducted through, which can be termed as digit '1' or '−1'. If different types of strains were applied, one FM layer would be spin-up half-metal, but the other would be the spin-down half-metal. There will be no electric current, which can be termed as the off state '0'. Purposely applying strains on the two FM layers (the 1T'-CrS$_2$ phase) output nine different information from the two-channel device in Fig. 6. By increasing the channel number n, we can get much more information than conventional charge-based devices: 3^n vs. 2^n.

In the end, we would like to discuss the feasibility of integrating different phases on one single piece of CrS$_2$ nanosheet for the spin-valve design. The first issue is the stability of the 2D heterostructure. Note that the thermodynamic stability and magnetic-state stability of individual phases under strains at the ambient condition have been discussed in the previous section. Two 2H/1T' and 1T/1T' heterostructures along the x- and y-direction are constructed in Supplementary Fig. 16. To further confirm the stability of the heterostructure, the ab initio molecular dynamics simulation was also performed at 300 K for 1 ps run as shown in Supplementary Fig. 17. Our DFT calculations show no structural change (phase transition) during the structure relaxation. This is consistent with a recent experiment in which the coexistence of 2H, 1T, and 1T' phases in a single CrS$_2$ nanosheet fabricated by the chemical vapor deposition (CVD) method was observed[33]. Fabricating the CrS$_2$ lateral heterostructures (Fig. 6) is thermodynamically feasible in experiments.

The second issue is the fabrication feasibility in experiments. In the past few years, there are significant advances in experimental techniques to fabricate 2D lateral heterostructure. For example, the MoTe$_2$/MoS$_2$ and WS$_2$/MoS$_2$ lateral heterostructures were fabricated using CVD[21,45,46]. Besides, 2H/1T' MoTe$_2$ lateral heterostructure was fabricated using CVD or chemical exfoliation methods[22,47]. It is reasonable to expect that a similar CVD growth technique can be employed to CrS$_2$ lateral heterostructure. Another promising option is to use some appropriate external stimuli to purposely induce phase transition in the local regions of a single-phase CrS$_2$ flake. There are plenty of studies in this regard for TMD materials. Supplementary Note 6 thoroughly discusses how to use strain to induce phase transition based on the results presented in Fig. 5. Some other options include electron doping[48,49], light or electron beam irradiation[50,51], chemical doping or alloying[52–55], as well as annealing and pressure[56,57].

In this paper, using DFT calculations, we systematically surveyed all IV, V, and VI group TMDs and identified CrS$_2$ as a material suitable for spintronic device designs. It has the most diverse electronic and magnetic properties that meet the requirements of
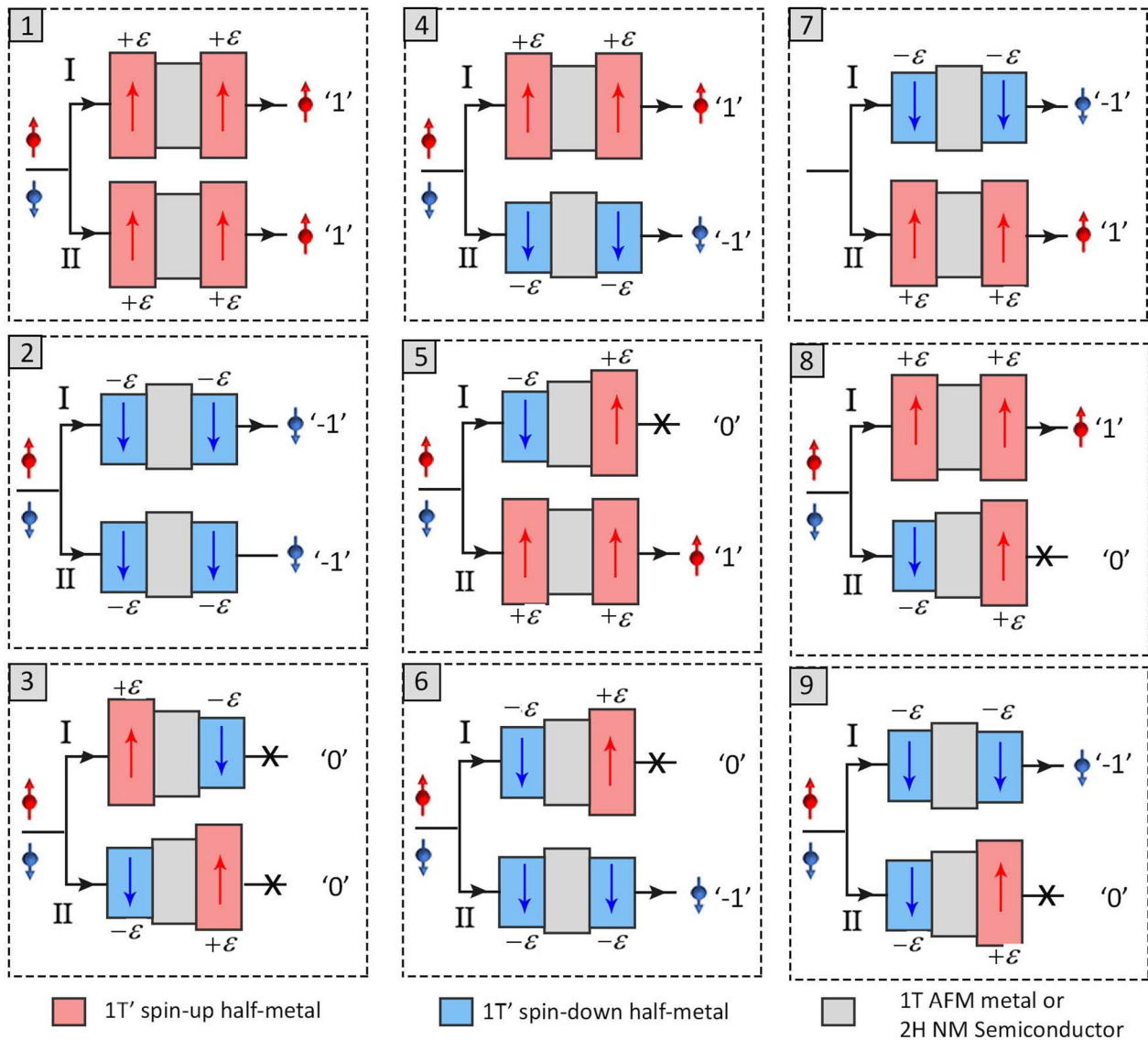
Fig. 6 A prototypical design of a strain-controlled spin-valve logic device with two channels. One 2D CrS_2 lateral heterostructure is one channel. There are two possible lateral heterostructures, $1T'/1T/1T'$ and $1T'/2H/1T'$. This design is analogous to the multi-channel 'universal memory' MRAM[8]. Strain can be used to switch spin-up or spin-down half-metal state in the two $1T'$ phase regions in one channel. By controlling the strains, either spin-up current, spin-down current, or no current can transport through the channel (see main text for details). The corresponding output can be defined as signal '1', '−1', and '0' for one channel. This two-channel device can output 9 different signals.

spintronics. It has a NM-SC (direct bandgap) 2H phase and an AFM metal 1T phase. Its $1T'$ phase shows FM ground state and is an indirect bandgap semiconductor with 0.26 and 1.92 eV for spin-up and spin-down electrons, respectively. The most interesting observation is that a uniaxial tensile or compressive strain along the y-direction can switch the $1T'$ phase into a spin-up or spin-down half-metallic state. This feature is particularly useful for spintronic device designs. As an example, a prototype spin-valve device is proposed based on 2D CrS_2 lateral heterostructure. This device is operated under strain instead of external magnetic fields. Besides, Cr-based compounds' 2D material such as CrX (X = N, P, As, Sb) show great potential possibility for spintronics device-related properties like half-metallic ferromagnets with high Curie temperature, anomalous Hall effect[58–60]. The features of such a 2D lateral heterostructure device based on Cr compounds, such as strain control, simple structure, and atomically sharp interface, could significantly reduce energy consumption, which remains a challenge in miniaturizing spintronic devices.

METHODS

Density functional theory calculation

Our DFT calculations were done using the Vienna Ab initio Simulation Package (VASP)[61]. The spin-polarized PBE exchange-correlation functional[62] and projector augmented wave method[63] were adopted for structure relaxation; the HSE06 method for the electronic structures and magnetic order[64]. The spin–orbit coupling (SOC) effect is not considered because the influence of SOC on band structure is negligible for CrS_2, as shown in Supplementary Fig. 19, which is also consistent with a previous study[33]. The 2D MX_2 layer was placed in the x–y plane. Periodic boundary condition was applied in all three directions. A vacuum space of at least 20 Å was applied along the z-direction to avoid the interaction between two periodic images. The cutoff energy was set to 400 eV. The Monkhorst-Pack k-point mesh[65] was set to $15 \times 11 \times 1$ for $1T'$-MX_2 primitive unit and $1 \times \sqrt{3} \times 1$ supercell of 2H/1T phase to keep cell k-point sampling spacing <0.04 Å^{-1} along with the supercell reciprocal vectors in the x–y plane. Atomic positions and lattice constants were fully relaxed until the total energy difference and forces were less than 10^{-4} eV and 0.005 eV Å^{-1}, respectively. A higher convergence criterion for total energy, 10^{-6} eV, was

adopted to perform self-consistent calculations and obtain electronic structures. The initial magnetic moment of a magnetic M atom was set to a high value (e.g., $5\,\mu_B$ for Cr) to ensure the automatic relaxation in DFT calculations could lead to the proper magnetic states.

The value of the in-plane uniaxial strain along the y-direction is defined as $\varepsilon_y = (b - b_0)/b_0 \times 100\%$, where b and b_0 are the in-plane lattice constants of the strained and unstrained 1T′ monolayers, respectively. CI-NEB calculations[66] were performed to estimate phase transition barriers of 2H–1T′ and 1T–1T′ transitions. The maximum residual forces of NEB calculations are $<0.01\,\mathrm{eV\,\mathring{A}^{-1}}$. Since NEB calculation cannot describe the magnetic order reversion process of 1T (AFM)–1T′ (FM) transition, we first calculated the NM 1T–1T′ transition process to approximate reaction coordinates. Then self-consistent calculation was performed on each coordinate with AFM and FM magnetic order. The magnetic order with lower total energy at each coordinate is adopted to approximately describe the energy barrier between 1T-AFM and 1T′-FM phases.

HSE06 and GGA + U examination

The PBE and HSE06 calculations show similar total energy order among the different phases (zero strain) of CrS_2 (Table 1), which is consistent with previous studies[31,33,67]. Thus, we adopted PBE functional to relax the crystal structure and adopted HSE06 for electronic structure calculations. We also tested the GGA + U method for CrS_2 (Supplementary Note 13). We did not adopt this method in this work for two reasons. First, the relative energy of 2H, 1T, and 1T′ phase with U_{eff} changing from 0 to 3.5 eV are shown in Supplementary Fig. 20a. The U_{eff} value significantly affects the stability (total energy difference) of the three phases. The 2H is the ground phase when $U_{eff} < 1$, but it will be the most unstable phase when $U_{eff} > 1$. Since many previous works concluded that 2H should be the ground state of CrS_2[30,32,67], the U_{eff} value should be smaller than 1. Second, the band structure of 1T′ with $U_{eff} = 0.5$ was calculated in Supplementary Fig. 20b. It shows a metal character, which is opposite to recent experimental results where the 1T′ phase has very low carrier mobility[33]. In contrast, for PBE and HSE06 calculations, our results show consistency for both phase stability and electronic structures with available experiments and other simulation works (Supplementary Note 14). Thus, these two functionals were adopted in this work.

DATA AVAILABILITY

The data that support the findings of this study are available from the corresponding author upon reasonable request.

REFERENCES

1. Wolf, S. A. et al. Spintronics: a spin-based electronics vision for the future. *Science* **294**, 1488–1495 (2001).
2. Han, W. Perspectives for spintronics in 2D materials. *APL Mater.* **4**, 032401 (2016).
3. Baibich, M. N. et al. Giant magnetoresistance of (001)Fe/(001)Cr magnetic superlattices. *Phys. Rev. Lett.* **61**, 2472–2475 (1988).
4. Moodera, J. S., Kinder, L. R., Wong, T. M. & Meservey, R. Large magnetoresistance at room temperature in ferromagnetic thin film tunnel junctions. *Phys. Rev. Lett.* **74**, 3273–3276 (1995).
5. Fan, Y. et al. Magnetization switching through giant spin-orbit torque in a magnetically doped topological insulator heterostructure. *Nat. Mater.* **13**, 699–704 (2014).
6. Mellnik, A. R. et al. Spin-transfer torque generated by a topological insulator. *Nature* **511**, 449–451 (2014).
7. Chappert, C., Fert, A. & Van Dau, F. The emergence of spin electronics in data storage. *Nat. Mater.* **6**, 813–823 (2007).
8. Åkerman, J. Toward a universal memory. *Science* **308**, 508–510 (2005).
9. Brataas, A., Kent, A. D. & Ohno, H. Current-induced torques in magnetic materials. *Nat. Mater.* **11**, 372–381 (2012).
10. Wang, M. et al. Field-free switching of a perpendicular magnetic tunnel junction through the interplay of spin–orbit and spin-transfer torques. *Nat. Electron.* **1**, 582–588 (2018).
11. Sander, D. et al. The 2017 magnetism roadmap. *J. Phys. D: Appl. Phys.* **50**, 363001 (2017).
12. Wang, W. G., Li, M., Hageman, S. & Chien, C. L. Electric-field-assisted switching in magnetic tunnel junctions. *Nat. Mater.* **11**, 64–68 (2011).
13. Shiota, Y. et al. Induction of coherent magnetization switching in a few atomic layers of FeCo using voltage pulses. *Nat. Mater.* **11**, 39–43 (2011).
14. Fusil, S., Garcia, V., Barthélémy, A. & Bibes, M. Magnetoelectric devices for spintronics. *Annu. Rev. Mater. Res.* **44**, 91–116 (2014).
15. Trieloff, M. et al. Structure and thermal history of the H-chondrite parent asteroid revealed by thermochronometry. *Nature* **422**, 502–506 (2003).
16. Chen, A. et al. Full voltage manipulation of the resistance of a magnetic tunnel junction. *Sci. Adv.* **5**, eaay5141 (2019).
17. Chen, A. et al. Giant nonvolatile manipulation of magnetoresistance in magnetic tunnel junctions by electric fields via magnetoelectric coupling. *Nat. Commun.* **10**, 243 (2019).
18. Yan, H. et al. A piezoelectric, strain-controlled antiferromagnetic memory insensitive to magnetic fields. *Nat. Nanotechnol.* **14**, 131–136 (2019).
19. Wang, M. et al. Strain-controlled giant magnetoresistance in spin valves grown on shape memory alloys. *ACS Appl. Electron. Mater.* **1**, 910–918 (2019).
20. Wang, L. et al. Morphology independent triplet formation in pentalene films: singlet fission as the triplet formation mechanism. *J. Chem. Phys.* **151**, 124701 (2019).
21. Chen, K. et al. Electronic properties of MoS_2–WS_2 heterostructures synthesized with two-step lateral epitaxial strategy. *ACS Nano* **9**, 9868–9876 (2015).
22. Zhang, X. et al. Low contact barrier in 2H/1T′ $MoTe_2$ in-plane heterostructure synthesized by chemical vapor deposition. *ACS Appl. Mater. Interfaces* **11**, 12777–12785 (2019).
23. Pereira, V. M. & Castro Neto, A.H. Strain engineering of graphene's electronic structure. *Phys. Rev. Lett.* **103**, 046801 (2009).
24. Liu, Z. et al. In-plane heterostructures of graphene and hexagonal boron nitride with controlled domain sizes. *Nat. Nanotechnol.* **8**, 119–124 (2013).
25. Kappera, R. et al. Phase-engineered low-resistance contacts for ultrathin MoS_2 transistors. *Nat. Mater.* **13**, 1128–1134 (2014).
26. Manzeli, S., Ovchinnikov, D., Pasquier, D., Yazyev, O. V. & Kis, A. 2D transition metal dichalcogenides. *Nat. Rev. Mater.* **2**, 17033 (2017).
27. Conley, H. J. et al. Bandgap engineering of strained monolayer and bilayer MoS_2. *Nano Lett.* **13**, 3626–3630 (2013).
28. Lv, H. Y., Lu, W. J., Shao, D. F., Liu, Y. & Sun, Y. P. Strain-controlled switch between ferromagnetism and antiferromagnetism in $1T-CrX_2(X = Se, Te)$ monolayers. *Phys. Rev. B* **92**, 214419 (2015).
29. Keum, D. H. et al. Bandgap opening in few-layered monoclinic $MoTe_2$. *Nat. Phys.* **11**, 482–486 (2015).
30. Ataca, C., Şahin, H. & Ciraci, S. Stable, single-layer MX_2 transition-metal oxides and dichalcogenides in a honeycomb-like structure. *J. Phys. Chem. C* **116**, 8983–8999 (2012).
31. Wang, C. et al. Layer and doping tunable ferromagnetic order in two-dimensional CrS_2 layers. *Phys. Rev. B* **97**, 245409 (2018).
32. Zhuang, H. L., Johannes, M. D., Blonsky, M. N. & Hennig, R. G. Computational prediction and characterization of single-layer CrS_2. *Appl. Phys. Lett.* **104**, 022116 (2014).
33. Habib, M. R. et al. Electronic properties of polymorphic two-dimensional layered chromium disulphide. *Nanoscale* **11**, 20123–20132 (2019).
34. Freitas, D. C. et al. Ferromagnetism in layered metastable 1T-$CrTe_2$. *J. Phys. Condens. Matter* **27**, 176002 (2015).
35. Castellanos-Gomez, A. et al. Local strain engineering in atomically thin MoS_2. *Nano Lett.* **13**, 5361–5366 (2013).
36. Azcatl, A. et al. Covalent nitrogen doping and compressive strain in MoS_2 by remote N2 plasma exposure. *Nano Lett.* **16**, 5437–5443 (2016).
37. Huang, C. et al. Ultra-high-temperature ferromagnetism in intrinsic tetrahedral semiconductors. *J. Am. Chem. Soc.* **141**, 12413–12418 (2019).
38. Zhang, L., Park, C. & Yoon, M. Quantum phase engineering of two-dimensional post-transition metals by substrates: toward a room-temperature quantum anomalous hall insulator. *Nano Lett.* **20**, 7186–7192 (2020).
39. Cheng, Y. C., Zhu, Z. Y., Mi, W. B., Guo, Z. B. & Schwingenschlögl, U. Prediction of two-dimensional diluted magnetic semiconductors: doped monolayer MoS_2 systems. *Phys. Rev. B* **87**, 100401 (2013).
40. Mogulkoc, A., Modarresi, M. & Rudenko, A. N. Two-dimensional chromium pnictides CrX $(X = P,As,Sb)$: half-metallic ferromagnets with high Curie temperature. *Phys. Rev. B* **102**, 024441 (2020).
41. Tehrani, S. et al. Magnetoresistive random access memory using magnetic tunnel junctions. *Proc. IEEE* **91**, 703–714 (2003).
42. Prinz, G. A. Magnetoelectronics. *Science* **282**, 1660–1663 (1998).
43. Ji, Y., Hoffmann, A., Jiang, J. S., Pearson, J. E. & Bader, S. D. Non-local spin injection in lateral spin valves. *J. Phys. D: Appl. Phys.* **40**, 1280–1284 (2007).
44. Katsnelson, M. I., Irkhin, V. Y., Chioncel, L., Lichtenstein, A. I. & de Groot, R. A. Half-metallic ferromagnets: from band structure to many-body effects. *Rev. Mod. Phys.* **80**, 315–378 (2008).

45. Gong, Y. et al. Vertical and in-plane heterostructures from WS_2/MoS_2 monolayers. *Nat. Mater.* **13**, 1135–1142 (2014).

46. Zhang, K. et al. Interlayer transition and infrared photodetection in atomically thin type-II $MoTe_2/MoS_2$ van der Waals heterostructures. *ACS Nano* **10**, 3852–3858 (2016).

47. Wang, D. et al. Phase engineering of a multiphasic 1T/2H MoS_2 catalyst for highly efficient hydrogen evolution. *J. Mater. Chem. A* **5**, 2681–2688 (2017).

48. Li, Y., Duerloo, K. A., Wauson, K. & Reed, E. J. Structural semiconductor-to-semimetal phase transition in two-dimensional materials induced by electrostatic gating. *Nat. Commun.* **7**, 10671 (2016).

49. Wang, Y. et al. Structural phase transition in monolayer $MoTe_2$ driven by electrostatic doping. *Nature* **550**, 487–491 (2017).

50. Kang, Y. et al. Plasmonic hot electron induced structural phase transition in a MoS_2 monolayer. *Adv. Mater.* **26**, 6467–6471 (2014).

51. Lin, Y. C., Dumcenco, D. O., Huang, Y. S. & Suenaga, K. Atomic mechanism of the semiconducting-to-metallic phase transition in single-layered MoS_2. *Nat. Nanotechnol.* **9**, 391–396 (2014).

52. Duerloo, K. A. & Reed, E. J. Structural phase transitions by design in monolayer alloys. *ACS Nano* **10**, 289–297 (2016).

53. Wang, Z. et al. Synthesizing 1T-1H two-phase $Mo_{1-x}W_xS_2$ monolayers by chemical vapor deposition. *ACS Nano* **12**, 1571–1579 (2018).

54. Tan, C. et al. Preparation of high-percentage 1T-phase transition metal dichalcogenide nanodots for electrochemical hydrogen evolution. *Adv. Mater.* **30**, 1705509 (2018).

55. Voiry, D. et al. Covalent functionalization of monolayered transition metal dichalcogenides by phase engineering. *Nat. Chem.* **7**, 45–49 (2015).

56. Yu, Y. et al. High phase-purity 1T'-MoS_2- and 1T'-$MoSe_2$-layered crystals. *Nat. Chem.* **10**, 638–643 (2018).

57. Xu, D. et al. Microwave-assisted 1T to 2H phase reversion of MoS_2 in solution: a fast route to processable dispersions of 2H-MoS_2 nanosheets and nanocomposites. *Nanotechnology* **27**, 385604 (2016).

58. Kuklin, A. V. et al. Two-dimensional hexagonal CrN with promising magnetic and optical properties: a theoretical prediction. *Nanoscale* **9**, 621–630 (2017).

59. Modarresi, M., Mogulkoc, A., Mogulkoc, Y. & Rudenko, A. N. Lateral spin valve based on the two-dimensional CrN/P/CrN heterostructure. *Phys. Rev. Appl.* **11**, 064015 (2019).

60. Mogulkoc, A., Modarresi, M. & Rudenko, A. N. Two-dimensional chromium bismuthate: a room-temperature Ising ferromagnet with tunable magneto-optical response. Preprint at https://arxiv.org/abs/2012.13625 (2020).

61. Kresse, G. & Furthmüller, J. Efficiency of ab-initio total energy calculations for metals and semiconductors using a plane-wave basis set. *Comput. Mater. Sci.* **6**, 15–50 (1996).

62. Perdew, J. P. et al. Atoms, molecules, solids, and surfaces: applications of the generalized gradient approximation for exchange and correlation. *Phys. Rev. B Condens. Matter* **46**, 6671–6687 (1992).

63. Blochl, P. E. Projector augmented-wave method. *Phys. Rev. B Condens. Matter* **50**, 17953–17979 (1994).

64. Heyd, J., Scuseria, G. E. & Ernzerhof, M. Hybrid functionals based on a screened Coulomb potential. *J. Chem. Phys.* **118**, 8207–8215 (2003).

65. Monkhorst, H. J. & Pack, J. D. Special points for Brillouin-zone integrations. *Phys. Rev. B* **13**, 5188–5192 (1976).

66. Henkelman, G., Uberuaga, B. P. & Jónsson, H. Influence of the exchange screening parameter on the performance of screened hybrid functionals. *J. Chem. Phys.* **113**, 9901 (2000).

67. Bastos, C. M. O., Besse, R., Da Silva, J. L. F. & Sipahi, G. M. Ab initio investigation of structural stability and exfoliation energies in transition metal dichalcogenides based on Ti-, V-, and Mo-group elements. *Phys. Rev. Mater.* **3**, 044002 (2019).

AUTHOR CONTRIBUTIONS

J.D., J.Z.L., and S.Y. designed the simulations and the framework of this research. K.C. carried out the first-principles calculations. Y.Y. carried out the phonon spectrum calculation and other detailed calculations. K.C., J.D., and J.Z.L. wrote the paper. Q.S. and T.C. interpreted the data and helped to draw figures. J.S. and X.D. performed some data analysis and provided many suggestions.

COMPETING INTERESTS

The authors declare no competing interests.

ADDITIONAL INFORMATION

Supplementary information The online version contains supplementary material available at https://doi.org/10.1038/s41524-021-00547-z.

Correspondence and requests for materials should be addressed to J.D., S.Y. or J.Z.L.

Reprints and permission information is available at http://www.nature.com/reprints

Publisher's note Springer Nature remains neutral with regard to jurisdictional claims in published maps and institutional affiliations.